2021-12-02

Late Ordovician climate change and extinctions driven by elevated volcanic nutrient supply

Longman, J

http://hdl.handle.net/10026.1/18128

1   **Late Ordovician climate change and extinctions driven by elevated volcanic nutrient**

2   **supply**

3

4   Jack Longman[1, 2,*], Benjamin J. W. Mills[3], Hayley R. Manners[4, 5], Thomas M. Gernon[4] and

5   Martin R. Palmer[4]

6   [1] Marine Isotope Geochemistry, Institute for Chemistry and Biology of the Marine

7   Environment (ICBM), University of Oldenburg, PO Box 2503, 26111 Oldenburg, Germany.

8   [2] School of Geography and the Environment, University of Oxford, South Parks Road,

9   Oxford, OX1 3QY, UK.

10   [3] School of Earth and Environment, University of Leeds, Leeds LS2 9JT, UK.

11   [4] School of Ocean and Earth Sciences, University of Southampton, Southampton, SO14 3ZH,

12   UK.

13   [5] School of Geography, Earth and Environmental Sciences, University of Plymouth,

14   Plymouth, PL4 8AA, UK.

15

16   [*]Corresponding Author: jack.longman@uni-oldenburg.de

17

18   **Abstract**

19   **The Late Ordovician (~459–444 million years ago) was characterised by global cooling,**

20   **glaciation and severe mass extinction. These events may have been driven by increased**

21   **delivery of the nutrient phosphorus (P) to the ocean, and associated increases in marine**

22   **productivity, but it is not clear why this occurred in the two pulses identified in the**

23   **geological record. We link both cooling phases, and the extinction, to volcanic eruptions**

24   **through marine deposition of nutrient-rich ash and the weathering of terrestrially**

25   **emplaced ash and lava. We then reconstruct the influence of Late Ordovician volcanic P**

26   **delivery on the marine system by coupling an estimate of bioavailable phosphate supply**

(derived from a depletion and weathering model) to a global biogeochemical model. Our model compares volcanic ash P content in marine sediments before and after alteration to determine depletion factors, and we find good agreement with observed carbon isotope and reconstructed temperature shifts. Hence, massive volcanism can drive substantial global cooling on million-year timescales due to P delivery associated with long-term weathering of volcanic deposits, offsetting the transient warming of greenhouse gas emission associated with volcanic eruptions. Such longer-term cooling and potential for marine eutrophication may be important for other volcanism-driven global events.

Main Text

The Late Ordovician mass extinction (LOME) occurred in two phases, and in terms of species loss was the second greatest extinction event in Earth's history[1–3]. The Late Ordovician is characterised by a number of carbon isotope excursions (CIEs), with two globally-represented, the Guttenburg (GICE) at ~454 Ma, and Hirnantian (HICE) at ~ 445 Ma[4]. The GICE coincides with global cooling, and the beginning of the HICE is associated with widespread glaciation, with the cooling periods generally implicated in instigating the LOME[1,5–7].

The primary driver behind the CIEs and associated cooling is uncertain. One possibility is that the emergence of early nonvascular land plants amplified terrestrial weathering and increased the delivery of the key limiting nutrient phosphorus to the oceans[8]. Greater availability of phosphorus increases marine productivity and organic carbon burial, driving a reduction in atmospheric CO_2 and a positive excursion in carbonate $\delta^{13}C$ (ref.[9]). Other proposals include an increasing fraction of eukaryotic marine production strengthening the biological pump[10], and increased tropical weathering resulting from orogenesis augmenting the supply of phosphorus to the oceans[11].

The concept that Late Ordovician cooling was driven by organic carbon burial is supported by observations[12], but why this occurred in two distinct pulses during the GICE and

52 HICE is unclear. This pulsing may have arisen from early plants colonising new terranes[8], but

53 there is little evidence for this, although poor fossil preservation cannot be ruled out[13]. Further,

54 the pace of early plant evolution remains highly uncertain[13] and there is no evidence that

55 eukaryotic evolution, or tropical uplift, occurred in distinct pulses. Existing global

56 biogeochemical models cannot reliably reproduce the Hirnantian glaciation (or isotope

57 excursions) associated with the HICE when based on known long-term tectonic cycles of uplift

58 and degassing, and the positioning of the continents[9], even though these models can accurately

59 reproduce the Permo-Carboniferous and late Cenozoic icehouses[9]. This suggests that the

60 Hirnantian icehouse was driven by some climatic forcing mechanism currently not well-

61 represented in these models.

62   Given the potential association between volcanism and global climate change[14,15], we

63 explore the concept that Late Ordovician marine productivity and cooling episodes were

64 directly related to subaerial volcanic activity. The Late Ordovician was characterised by

65 extensive volcanic eruptions, preserved in the sedimentary record as bentonites[16,17]. These

66 bentonites represent some of the largest volcanic eruptions in Earth's history, with estimates

67 indicating some of the better studied events (Millbrig, Deicke and Kinnekulle) erupted $\geq$1000

68 km^3 of pyroclastic material[18]. In addition, there are hundreds of spatially extensive bentonites

69 of Late Ordovician (459 – 444 Ma) age preserved across North America[19], Northern Europe[20],

70 and China[16,21], prompting suggestions of a causal link between volcanism and global cooling

71 during this period[3,14,17]. Most recently, several studies have employed the total organic carbon

72 to mercury ratio (TOC/Hg), to directly link volcanic Hg emission to Late Ordovician climatic

73 change (e.g. refs.[22,23]). However, it remains uncertain whether cooling was driven by rapid

74 sulfate emissions, through the immediate weathering of ash and lava, or by longer-term

75 weathering of volcanic arcs and uplifted terranes[17,23], a problem compounded by poorly

76 constrained volcanic fluxes.

77   Volcanism may cool the climate on non-transitory timescales due to enhanced

78   productivity and organic carbon preservation[24], with one of the key drivers being enhanced P

79   supply derived from leaching of volcanic ash[25]. It is not currently clear how much P may have

80   been supplied from ash during the Late Ordovician, or how input of volcanic P may have

81   influenced the marine environment. To answer these questions, we compile global data on P

82   depletion in tephra layers today, as a method of quantifying P release to the ocean during ash

83   deposition and diagenesis. We couple our estimates of P flux to a global biogeochemical model

84   to investigate the potential impact of such nutrient supply to the Late Ordovician marine carbon

85   cycle.

86   **Timing and extent of volcanism during the Late Ordovician**

87   To estimate timing of volcanic activity, we compile 43 Ar-Ar and U-Pb dates from

88   North American and Scandinavian bentonites (Fig. 1a), and 24 dates from Chinese bentonites

89   of Late Ordovician age (Fig. 1b). Our reconstruction indicates that bentonite deposition

90   occurred in two discrete pulses (Fig. 1c), corresponding to the eruption of two geographically

91   distinct volcanic provinces (Figure 2). The first pulse represents North American/Scandinavian

92   volcanism and is well-constrained, with the greatest depositional intensity occurring between

93   454.5 – 453 Ma, peaking at 453.5 Ma (Fig. 1c). This peak primarily represents highly-precise

94   measurements of the North American "big" bentonites, the Deicke and Millbrig[5,26], and the

95   Grimstorp bentonite[26]. A slightly earlier peak is also apparent (c. 456.5 Ma), representing

96   potentially uncertain estimates of the Kinnekulle bentonite age[27], and other unnamed bentonites

97   from Oslo[20] (see Supplementary Table 4). Chinese bentonite ages exhibit more spread, with

98   fewer highly precise dates (Fig. 1c). Our compilation suggests the most intense volcanism in

99   the China region occurred between 445.25 – 442.5 Ma, with a peak at about 444 Ma (Fig. 1c),

100   corresponding to some of the most accurate dates from outcrop in the south-western Yunnan

101   province[28], and central Hubei province[29]. These two volcanic pulses correspond well to the two

102   primary carbon isotope excursions of the Late Ordovician, the GICE and HICE, and may thus

103   support a link between volcanism and climate change.

104   **P release during ash deposition, diagenesis and weathering**

105   To investigate this hypothesis, we estimate the amount of P which may have been

106   supplied by the two main pulses of volcanism. To estimate the percentage of P released during

107   ash deposition and diagenesis, altered ash compositions are compared to unaltered protolith

108   compositions to estimate metal mobility[30,31], using protolith data from the GEOROC database

109   (http://georoc.mpch-mainz.gwdg.de) and our data from altered tephras (see Methods).

110   Specifically, marine sediment-hosted tephras from the Lesser Antilles and the Aleutian arcs

111   have been analysed and compared to similar data from eight additional modern volcanic

112   provinces (Fig. 1). In addition to direct input of P from volcanic ash deposition, the

113   emplacement and subsequent terrestrial weathering of extensive ash beds would have led to a

114   secondary source of P to the oceans. The scale of this P flux has been estimated from a Monte

115   Carlo simulation of inputs using published variables including the number, and scale of

116   eruptions (Methods, Extended Data Figures 1, 2).

117   Depletion factors indicate between 31% (mean) and 48% (median) of the P originally

118   hosted in tephra is lost during early diagenesis (Fig. 3). The potential scale of this process is

119   calculated in the modern oceans, using an average of 1.14 ± 0.6 km^3 ash deposited per year,

120   with 70 ± 7.5 % falling into the ocean[31], an ash density of 1400 ± 130 kg/m^3 (ref.[32]), and an

121   original P content in tephra of 0.41 ± 0.19 wt% (ref.[33]). For each variable, a Monte Carlo-based

122   approach is applied, using the average and standard deviation to develop 10,000 possible

123   iterations of each variable. From this calculation, the most likely annual P flux from ash

124   deposition and diagenesis is estimated to be approximately 3×10^{10} mol P yr^{-1}. This is similar

125   to estimates of global dust input to the P cycle today (3.2×10^{10} mol P yr^{-1}), and exceeds the

126   dissolved riverine input ($0.6 - 1.1 \times 10^{10}$ mol P yr^{-1}; ref.[34]). Present-day volcanism is thought

127   to be far smaller in scale than in periods such as the Ordovician[35,36]. Therefore, enhanced P

128   supply tied to volcanism likely played an even more important role in biogeochemical cycles

129   of P during the Ordovician.

130   **Impact of volcanic ash supply on Late Ordovician climate**

131   The depletion factors and estimates of ash supply during the Late Ordovician can be

132   used to quantify the scale of P supply during the two studied events. For the GICE, our

133   simulations indicate a mean of 2.29×10^{15} mol P (Fig. 4), which increases to 6.49×10^{15} mol P

134   in the upper estimates of the simulations (95th percentile). For the volcanic episode covering the

135   HICE, our simulations suggest a mean supply of 2.89×10^{15} mol P, with an upper estimate of

136   8.24×10^{15} mol P (95th percentile) (Fig. 4). In addition to ash falling into the ocean, the impact

137   of erosion of terrestrially emplaced ash and lava on the P cycle is considered by estimating

138   weathering fluxes of P (Methods). Newly emplaced ashes and basaltic rocks weather

139   rapidly[37,38], such that in Earth's modern configuration, despite representing only $3 - 5\%$ of land

140   area, chemical weathering of basalt contributes ~30% of the total CO_2 consumption by silicate

141   weathering[37,38]. Our approach to quantifying the impact of this process results in a mean

142   additional (riverine) P flux from weathering of 7.51×10^{14} mol P Myr^{-1} in the millennia after

143   emplacement (Fig. 4c), with an upper estimate of 1.23×10^{15} mol P Myr^{-1} (95th percentile),

144   providing another source of bioavailable P to the ocean system.

145   The impact of this level of volcanic nutrient supply on Ordovician climate is estimated

146   using the COPSE global biogeochemical model[39]. The GICE and HICE P inputs are represented

147   by Gaussian functions with their maxima at the times of highest depositional intensity noted

148   above (i.e., 453.5 and 444 Ma) and with a width of 2 Myrs, constrained in part by the duration

149   of the carbon isotope excursions. The total P input is calculated for both the means and 95th

150   percentiles and is summed from the P depletion model and weathering inputs. A further factor

151   is also added into the P delivery calculation to represent the recycling of P from sediments,

152   because P loading and eutrophication in marginal settings leads to a substantial recycling flux

153   of P from the sediments[40], due to the increase in anaerobic processing of organic matter and the

154   scarcity of Fe(III) phases that scavenge P. The COPSE model does not represent these

155   feedbacks well, because it has a well-mixed global ocean and no consideration of continental

156   margins, with substantial recycling of P relying on eutrophication of the global ocean rather

157   than productive shelves and slope environments alone[39]. This is relevant to the Ordovician, a

158   time when sea level was perhaps 300 m higher than present[41], with extensive shelf

159   environments[42]. Hence, parallel experiments were run to determine the degree to which P

160   recycling is dampened in COPSE versus a published P cycle model in which the shelves are

161   considered separately (see Methods, ref.[43]). We conclude that a 5-fold larger P input is required

162   in COPSE to produce the same spike in marine P concentration observed in the multi-box model

163   (Extended Data Figure 3). Thus, P inputs in the additional COPSE simulations are increased 5-

164   fold to represent both the initial input and the additional recycling of P. The large size of this

165   factor is related to the relatively small size of the ocean shelves (as a fraction of the whole

166   ocean) compared to their disproportionately large contribution to organic matter burial.

167   An important parameter in COPSE is the degree to which land plants amplify

168   continental weathering rates. This value is poorly constrained and is typically varied in

169   sensitivity analyses between around 2- and 7-fold, giving a wide range of possible background

170   CO_2 concentrations for the early Palaeozoic[44]. We choose a factor 2 enhancement for the model

171   runs in this work, which gives a relatively low background Ordovician CO_2 concentration of

172   around 1000 ppm, consistent with more recent proxy data[45]. Other than the new P inputs and

173   choice of biotic weathering parameter, the model remains identical to the long-term baseline

174   shown in ref.[39]. Figure 5 shows the model outputs for atmospheric CO_2, average surface

175   temperature, marine anoxia, and the $\delta^{13}C$ of new sedimentary carbonates. The model outputs

176   show that the P release from volcanic ash deposition and weathering, combined with the

177   recycling of P from sediments, is sufficient to cause large-scale changes in climate and

178 biogeochemistry as observed in the geological record[10,14]. In the "95th percentile + recycling"

179 input scenario, carbon isotope excursions of ~3‰ and ~4‰ are predicted, which are

180 synchronous with the GICE and HICE, respectively, and are of similar magnitude. In this

181 scenario, maximum global cooling at the HICE is around 3°C, and a global average surface

182 temperature of below 15°C is reached at the nadir. These temperature predictions are in line

183 with clumped isotope thermometry which suggests the Hirnantian icehouse was relatively short

184 lived and represented a similar global average temperature to recent Pleistocene glaciation[6,46].

185 The extent of marine anoxia increases during the P input events in the model, although

186 given the global well-mixed ocean in the model, shelf anoxia would be expected to increase by

187 a larger fraction than the global ocean. This is against a backdrop of marine oxygenation

188 through the Ordovician and Silurian predicted by COPSE[39]. One of the major features of the

189 HICE in the geological record is the widespread formation of organic-rich shales, in particular

190 in China[47,48], potentially linked to widespread ocean anoxia[10,49]. In COPSE, the relative increase

191 in anoxia is much larger during the HICE – close to a doubling in the "95th percentile +

192 recycling" scenario.

Implications for the LOME

194 Our model results suggest that volcanic ash diagenesis and weathering of erupted

195 products likely played a key role in the Late Ordovician Earth system. In order to reproduce the

196 magnitude of Earth system change, we require that these inputs are at the 95th percentile of our

197 analysis. However, given the relatively sparse nature of the geological record of the Palaeozoic,

198 and the conservative approach utilised here to derive estimates of P supply from ash (Methods),

199 we stress that our analysis likely underestimates the number of volcanic events. This is

200 supported by the close comparison between the model output of the "95th percentile +

201 recycling" input scenario and proxy data (Fig. 5, ref.[50]). Our results may explain several features

202 of the LOME, which do not follow trends associated with other mass extinctions, in particular

203 their link to cooling, rather than warming. Volcanic activity has been invoked as the driver

204 behind a number of short-term climatic upheavals and mass extinctions[51], including those at the

205 end of the Permian[52] and in the Triassic periods[53], resulting in the rapid fluctuations between

206 icehouse and greenhouse conditions known to stress faunas and drive biodiversity loss[3,52].

207   For the Late Ordovician, it appears that the long-term nature of nutrient supply from

208 weathering of eruptive products such as volcanic ash plays a more dominant role than the

209 medium-term warming associated with CO_2 injection. When comparing to climatic change, it

210 is clear that the first stepped decrease in faunal diversity occurred soon after the GICE, with

211 two further decreases occurring temporally close to the HICE[3,54]. Our approach considers many

212 eruptions to estimate nutrient supply on a coarse scale. The super-eruptions represented by

213 bentonites would likely have led to initial cooling (due to injection of stratospheric aerosols),

214 followed by warming (from CO_2 injection), before cooling because of increases in nutrient

215 supply and associated productivity levels. The warming/cooling cycles this scenario represents

216 are purportedly dangerous for organisms, with biodiversity loss occurring when temperatures

217 fall outside the optimal window[3], potentially explaining the LOME initiation. Due to their

218 global nature, we focus on the HICE and GICE, and only model two P pulses. However,

219 bentonite ages suggest that multiple eruptions occurred between the two largest volcanic

220 episodes and CIEs (Fig. 1), which may have led to transient local CIEs, such as those reported

221 in the Scandinavian sections[7].

222   In addition to releasing nutrients, it is possible that other toxic metals are also released

223 during ash alteration and diagenesis[25]. During the Hirnantian glaciation and the HICE, there is

224 evidence for metal-induced malformations in fossil plankton assemblages[55]. Further, volcanic

225 ash may lead to the formation of large-scale anoxic conditions below deposited blankets[24],

226 which may have further enhanced redox-based recycling of toxic metals[55] and led to the

227 deposition of widespread black shales[47]. Using the evidence presented here, we conclude that

228   the pulsed nature of global cooling at this time appears to be a result of the eruption of two

229   distinct volcanic provinces, one in what is now North America and the Baltic, and one in what

230   is now Southern China. Further, our models suggest that the deposition of extensive ash

231   blankets and weathering of lavas emplaced during Late Ordovician volcanism, supplied

232   sufficient P to drive global cooling, glaciation, and the LOME.

241   **Author Contributions**

242   J.L., T.M.G. and M.R.P. conceived this research. J.L. and H.R.M. completed the laboratory

243   analyses. B.J.W.M. completing the modelling and J.L. compiled and analysed the data. J.L. and

244   B.J.W.M. created the figures. J.L. and B.J.W.M. wrote the manuscript, with input from T.M.G.,

245   H.R.M. and M.R.P.

246   **Competing Interests**

247   The authors declare no competing interests.

248   **Corresponding Author**

249   All correspondence and request for materials should be addressed to Jack Longman

250   (jack.longman@uni-oldenburg.de)

Figure Captions

Figure 1: Compilation of Late Ordovician bentonite ages from North America and China.
Bentonites ages in North America/Scandinavia (**a**), and China (**b**). Each age is represented by a probability density curve derived from published mean and standard deviation, from which 10,000 Monte Carlo simulations were completed and binned at 0.25 Myr intervals to attain probability densities of the eruption occurring in each bin. Colours correspond to the studies from which each age is obtained. **c**, Average probability densities for each 0.25 Myr bin, for the North American (blue) and Chinese bentonites (red). Vertical lines indicate the bin in which bentonite deposition is most likely. (See Supplementary Tables 4 and 5 for references).

Figure 2: Paleogeographic reconstruction for the Late Ordovician at c. 450 Ma (Katian).
Marked with ellipses are the two volcanic provinces investigated in this study, with blue ellipses representing the North American and Scandinavian province, and a green ellipse to represent the Chinese province. The base map was constructed using the plate tectonic reconstructions from ref.[56] and is based partly on ref[57].**Figure 3: Box and whisker diagrams of phosphorus depletion, an indicator of the amount of phosphorus lost to the ocean, from ten present-day representative volcanic provinces (a).** Boxes are defined between the first and third quartile (the interquartile range, IQR), with minimum and maximum whiskers representative of 1.5 times the IQR. Also shown is a map of each volcanic province used for this reconstruction (**b**), with the provinces identified by numbers given in panel (**a**).**Figure 4: Monte Carlo simulations of phosphorus supply from volcanic weathering during the Late Ordovician, with variable distributions defined by our ash depletion and weathering model.** (**a**) and (**b**) represent P supply from ash deposition and diagenesis. In both panels, the total ash volume is presented along the x-axis, with total phosphorus supply on the y-axis. Each Monte Carlo simulation is indicated by a circle, with the colour indicating the depletion factor. (**c**) Estimate of P flux resulting from weathering of terrestrial volcanic matter (y-axis), plotted against the

276 area covered by this ash and lava. Again, each simulation is indicated by a filled circle, with

277 the colour denoting the rate of phosphorus supply.

278 **Figure 5. Biogeochemical model outputs for impacts of volcanism during the GICE and**

279 **HICE.** COPSE model baseline runs[39] plus P supply from ash. **a**, Grey lines show the P input

280 Gaussian functions (see text). The P input magnitude follows the mean or 95th percentiles of

281 the values derived for ash supply and weathering combined, with or without recycling of P from

282 sediments (see main text). **b**, Modelled δ^{13}C of carbonates (with colours defined in panel e)

283 compared to data[50] (yellow circles). **c**, Modelled atmospheric CO_2. **d**, Modelled global average

284 surface temperature. **e**, Degree of marine anoxia (represented as the modelled proportion of

285 anoxic seafloor). Solid lines show the same simulations as the dashed lines, but with additional

286 P input to represent sedimentary recycling of P (see text).

287 **References**

288 1.   Harper, D. A. T., Hammarlund, E. U. & Rasmussen, C. M. Ø. End Ordovician extinctions: A

289 coincidence of causes. Gondwana Res. 25, 1294–1307 (2014).

290 2.   Bambach, R. K., Knoll, A. H. & Wang, S. C. Origination, extinction, and mass depletions of

291 marine diversity. Paleobiology 30, 522–542 (2004).

292 3.   Rasmussen, C. M. Ø., Kröger, B., Nielsen, M. L. & Colmenar, J. Cascading trend of Early

293 Paleozoic marine radiations paused by Late Ordovician extinctions. Proc. Natl. Acad. Sci. U. S. A. 116,

294 7207–7213 (2019).

295 4.   Bergström, S. M., Schmitz, B., Saltzman, M. R. & Huff, W. D. The Upper Ordovician

296 Guttenberg δ13C excursion (GICE) in North America and Baltoscandia: Occurrence,

297 chronostratigraphic significance, and paleoenvironmental relationships. Geol. Soc. Am. Spec. Pap. 466,

298 37–67 (2010).

299   5.   Metzger, J. G., Ramezani, J., Bowring, S. A. & Fike, D. A. New age constraints on the duration
300   and origin of the Late Ordovician Guttenberg $\delta^{13}C_{carb}$ excursion from high-precision U-Pb
301   geochronology of K-bentonites. GSA Bull. (2020) doi:10.1130/B35688.1.

302   6.   Finnegan, S. et al. The magnitude and duration of late Ordovician-early Silurian glaciation.
303   Science. 331, 903–906 (2011).

304   7.   Ainsaar, L. et al. Middle and Upper Ordovician carbon isotope chemostratigraphy in
305   Baltoscandia: A correlation standard and clues to environmental history. Palaeogeogr. Palaeoclimatol.
306   Palaeoecol. 294, 189–201 (2010).

307   8.   Lenton, T. M., Crouch, M., Johnson, M., Pires, N. & Dolan, L. First plants cooled the
308   Ordovician. Nat. Geosci. 5, 86–89 (2012).

309   9.   Mills, B. J. W. et al. Modelling the long-term carbon cycle, atmospheric CO2, and Earth surface
310   temperature from late Neoproterozoic to present day. Gondwana Research vol. 67 172–186 (2019).

311   10.   Shen, J. et al. Improved efficiency of the biological pump as a trigger for the Late Ordovician
312   glaciation. Nat. Geosci. 11, 510–514 (2018).

313   11.   Swanson-Hysell, N. L. & Macdonald, F. A. Tropical weathering of the Taconic orogeny as a
314   driver for Ordovician cooling. Geology 45, 719–722 (2017).

315   12.   Bartlett, R. et al. Abrupt global-ocean anoxia during the Late Ordovician–early Silurian detected
316   using uranium isotopes of marine carbonates. Proc. Natl. Acad. Sci. U. S. A. 115, 5896–5901 (2018).

317   13.   Morris, J. L. et al. The timescale of early land plant evolution. Proc. Natl. Acad. Sci. U. S. A.
318   115, E2274–E2283 (2018).

319   14.   Buggisch, W. et al. Did intense volcanism trigger the first Late Ordovician icehouse? Geology
320   38, 327–330 (2010).

321   15.   Herrmann, A. D., Leslie, S. A. & MacLeod, K. G. Did intense volcanism trigger the first Late
322   Ordovician icehouse?: COMMENT. Geology 39, e237–e237 (2011).

323 16. Huff, W. D., Bergström, S. M. & Kolata, D. R. Ordovician explosive volcanism. Geol. Soc.

324 Am. Spec. Pap. 466, 13–28 (2010).

325 17. Tao, H., Qiu, Z., Lu, B., Liu, Y. & Qiu, J. Volcanic activities triggered the first global cooling

326 event in the Phanerozoic. J. Asian Earth Sci. 104074 (2019) doi:10.1016/j.jseaes.2019.104074.

327 18. Huff, W. D., Kolata, D. R., Bergström, S. M. & Zhang, Y. S. Large-magnitude Middle

328 Ordovician volcanic ash falls in North America and Europe: Dimensions, emplacement and post-

329 emplacement characteristics. J. Volcanol. Geotherm. Res. 73, 285–301 (1996).

330 19. Sell, B. K. et al. Stratigraphic correlations using trace elements in apatite from late Ordovician

331 (Sandbian-Katian) K-bentonites of eastern North America. Bull. Geol. Soc. Am. 127, 1259–1274

332 (2015).

333 20. Ballo, E. G., Augland, L. E., Hammer, Ø. & Svensen, H. H. A new age model for the Ordovician

334 (Sandbian) K-bentonites in Oslo, Norway. Palaeogeogr. Palaeoclimatol. Palaeoecol. 520, 203–213

335 (2019).

336 21. Liu, W. et al. K-bentonites in Ordovician-Silurian transition from South China: Implications for

337 tectonic evolution in the northern margin of Gondwana. J. Geol. Soc. London. jgs2020-049 (2020)

338 doi:10.1144/jgs2020-049.

339 22. Smolarek-Lach, J., Marynowski, L., Trela, W. & Wignall, P. B. Mercury Spikes Indicate a

340 Volcanic Trigger for the Late Ordovician Mass Extinction Event: An Example from a Deep Shelf of the

341 Peri-Baltic Region. Sci. Rep. 9, 1–11 (2019).

342 23. Jones, D. S., Martini, A. M., Fike, D. A. & Kaiho, K. A volcanic trigger for the late Ordovician

343 mass extinction? Mercury data from south China and Laurentia. Geology 45, 631–634 (2017).

344 24. Longman, J., Palmer, M. R., Gernon, T. M. & Manners, H. R. The role of tephra in enhancing

345 organic carbon preservation in marine sediments. Earth-Science Rev. 192, 480–490 (2019).

346   25.   Jones, M. T. & Gislason, S. R. Rapid releases of metal salts and nutrients following the

347   deposition of volcanic ash into aqueous environments. Geochim. Cosmochim. Acta 72, 3661–3680

348   (2008).

349   26.   Sell, B., Ainsaar, L. & Leslie, S. Precise timing of the Late Ordovician (Sandbian) super-

350   eruptions and associated environmental, biological, and climatological events. J. Geol. Soc. London.

351   170, 711–714 (2013).

352   27.   Tucker, R. D. & McKerrow, W. S. Early Paleozoic chronology: a review in light of new U-Pb

353   zircon ages from Newfoundland and Britain. Can. J. Earth Sci. 32, 368–379 (1995).

354   28.   Ling, M. X. et al. An extremely brief end Ordovician mass extinction linked to abrupt onset of

355   glaciation. Solid Earth Sci. 4, 190–198 (2019).

356   29.   Du, X. et al. Was volcanic activity during the Ordovician-Silurian transition in South China part

357   of a global phenomenon? Constraints from zircon U–Pb dating of volcanic ash beds in black shales.

358   Mar. Pet. Geol. 114, 104209 (2020).

359   30.   Lee, C.-T. A. et al. Volcanic ash as a driver of enhanced organic carbon burial in the Cretaceous.

360   Sci. Rep. 8, 4197 (2018).

361   31.   Longman, J., Palmer, M. R., Gernon, T. M. & Manners, H. R. Subaerial volcanism is a major

362   contributor to oceanic iron and manganese cycles. In Review.

363   32.   Gudmundsson, M. T. et al. Ash generation and distribution from the April-May 2010 eruption

364   of Eyjafjallajökull, Iceland. Sci. Rep. 2, 572 (2012).

365   33.   Laeger, K. et al. High-resolution geochemistry of volcanic ash highlights complex magma

366   dynamics during the Eyjafjallajökull 2010 eruption. Am. Mineral. 102, 1173–1186 (2017).

367   34.   Paytan, A. & McLaughlin, K. The oceanic phosphorus cycle. Chem. Rev. 107, 563–576 (2007).

368   35.   Cao, W., Lee, C. T. A. & Lackey, J. S. Episodic nature of continental arc activity since 750 Ma:

369   A global compilation. Earth Planet. Sci. Lett. 461, 85–95 (2017).

370 36.   Mills, B. J. W., Scotese, C. R., Walding, N. G., Shields, G. A. & Lenton, T. M. Elevated CO2

371 degassing rates prevented the return of Snowball Earth during the Phanerozoic. Nat. Commun. 8, 1–7

372 (2017).

373 37.   Dessert, C., Dupré, B., Gaillardet, J., François, L. M. & Allègre, C. J. Basalt weathering laws

374 and the impact of basalt weathering on the global carbon cycle. Chem. Geol. 202, 257–273 (2003).

375 38.   Dessert, C. et al. Erosion of Deccan Traps determined by river geochemistry: impact on the

376 global climate and the 87Sr/86Sr ratio of seawater. Earth Planet. Sci. Lett. 188, 459–474 (2001).

377 39.   Tostevin, R. & Mills, B. J. W. Reconciling proxy records and models of Earth's oxygenation

378 during the Neoproterozoic and Palaeozoic. Interface Focus 10, 20190137 (2020).

379 40.   Slomp, C. P. & Van Cappellen, P. The global marine phosphorus cycle: sensitivity to oceanic

380 circulation. Biogeosciences 4, 155–171 (2007).

381 41.   Hallam, A. Phanerozoic sea-level changes. (Columbia Univeristy Press, 1992).

382 42.   Walker, L. J., Wilkinson, B. H. & Ivany, L. C. Continental drift and phanerozoic carbonate

383 accumulation in shallow-shelf and deep-marine settings. J. Geol. 110, 75–87 (2002).

384 43.   Alcott, L. J., Mills, B. J. W. & Poulton, S. W. Stepwise Earth oxygenation is an inherent property

385 of global biogeochemical cycling. Science. 366, 1333–1337 (2019).

386 44.   Berner, R. A. A model for atmospheric CO 2 over Phanerozoic time. Am. J. Sci. 291, 339–376

387 (1991).

388 45.   Witkowski, C. R., Weijers, J. W. H., Blais, B., Schouten, S. & Sinninghe Damsté, J. S.

389 Molecular fossils from phytoplankton reveal secular PCO2 trend over the phanerozoic. Sci. Adv. 4,

390 eaat4556 (2018).

391 46.   Goldberg, S. L., Present, T. M., Finnegan, S. & Bergmann, K. D. A high-resolution record of

392 early Paleozoic climate. Proc. Natl. Acad. Sci. 118, (2021).

393 47.   Zou, C. et al. Organic-matter-rich shales of China. Earth-Science Reviews vol. 189 51–78

394 (2019).

395   48.   Su, W. et al. K-bentonite, black-shale and flysch successions at the Ordovician-Silurian

396   transition, South China: Possible sedimentary responses to the accretion of Cathaysia to the Yangtze

397   Block and its implications for the evolution of Gondwana. Gondwana Res. 15, 111–130 (2009).

398   49.   LaPorte, D. F. et al. Local and global perspectives on carbon and nitrogen cycling during the

399   Hirnantian glaciation. Palaeogeogr. Palaeoclimatol. Palaeoecol. 276, 182–195 (2009).

400   50.   Saltzman, M. R. & Thomas, E. Carbon isotope stratigraphy. in The Geologic Time Scale 2012

401   (eds. Gradstein, F. M., Ogg, J.., Schmitz, M. D. & Ogg, G, M.) 207–232 (Elsevier, 2012).

402   doi:10.1016/B978-0-444-59425-9.00011-1.

403   51.   Sobolev, S. V. et al. Linking mantle plumes, large igneous provinces and environmental

404   catastrophes. Nature 477, 312–316 (2011).

405   52.   Black, B. A. et al. Systemic swings in end-Permian climate from Siberian Traps carbon and

406   sulfur outgassing. Nat. Geosci. 11, 949–954 (2018).

407   53.   Schoene, B., Guex, J., Bartolini, A., Schaltegger, U. & Blackburn, T. J. Correlating the end-

408   Triassic mass extinction and flood basalt volcanism at the 100 ka level. Geology 38, 387–390 (2010).

409   54.   Fan, J. X. et al. A high-resolution summary of Cambrian to early Triassic marine invertebrate

410   biodiversity. Science . 367, 272–277 (2020).

411   55.   Vandenbroucke, T. R. A. et al. Metal-induced malformations in early Palaeozoic plankton are

412   harbingers of mass extinction. Nat. Commun. 6, (2015).

413   56.   Merdith, A. S. et al. Extending full-plate tectonic models into deep time: Linking the

414   Neoproterozoic and the Phanerozoic. Earth-Science Rev. 214, 103477 (2021).

415   57.   Cocks, L. R. M. & Torsvik, T. H. Ordovician palaeogeography and climate change. Gondwana

416   Res. (2020) doi:10.1016/j.gr.2020.09.008.

417

Methods

Major and trace element geochemistry

Tephra layers from IODP cores 1396C (Lesser Antilles) and U1339D (Bering Sea) were analysed for their phosphorus content. Tephras were identified visually, and microscopically, in core 1339D and through their low $CaCO_3$ content in U1396C. P was analysed in tephra layers after mixed acid (HNO_3-HCl-HF) bench-top digestion. Samples were then analysed on a Perkin Elmer 2000B at the University of Oxford. Analysis was completed in both standard mode (m/z 31) and in reaction mode, with O_2 as reaction gas and analysis on m/z 47. In all cases, data were more accurate and detection limits were sufficient from standard mode analysis and so we present these results here. Blanks and standards (BHVO2 basalt) were prepared and analysed in the same manner (Supplementary Table 1). For cores U1396C and U1339D, Al and Zr were determined after digestion using the same procedure as above, again alongside standard BHVO2 and blanks. Concentrations of these elements were determined using a Thermo X-Series ICP-MS at the University of Southampton (Supplementary Table 1).

P depletion factors and P release

We used the GEOROC database to estimate the protolith composition of volcanic material from each of the source regions. These data were filtered to remove any data related to non-outcrop samples, xenoliths and any mineral-specific analyses. This database was used to estimate the composition of tephra prior to dissolution and diagenetic alteration. By normalising P to Zr and plotting this ratio against Ti/Zr (elements which are largely immobile during diagenesis), the empirical relationship between the two ratios can be used to estimate the original protolith composition following the method of ref.[30], developed to estimate metal mobility in Cretaceous tephras (Supplementary Table 2). The linear regression representing this relationship is then used back-calculate the original composition of altered tephra

442   (Supplementary Tables 2, 3, refs.[58–64]). These compositions, along with compositions of altered

443   tephra, are then used to calculate depletion factors using the following equation (Equation 1):

444
$$P_D = \frac{M_P^L}{M_P^O} = 1 - \frac{\left(\frac{C_P^{re}}{C_{Zr}^{re}}\right)}{\left(\frac{C_P^O}{C_{Zr}^O}\right)} \text{ (Eq. 1)}$$

445   The left side of the equation is the depletion factor, where M_P^O original P mass in the protolith,

446   M_P^L is the loss of P. C_P^{re} and C_{Zr}^{re} are the mass of P and Zr in tephra, and C_P^O/C_{Zr}^O represents the

447   ratio of P to Zr in the protolith, back-calculated from the linear regression of GEOROC data

448   (Fig. 3, Extended Data Figures 1, 2).

449   **Estimating the extent and timing of volcanism during the Late Ordovician**

450   We use Monte Carlo simulations of variables associated with bentonite deposition

451   during the Late Ordovician to estimate the size of the volcanic eruptions and associated ash

452   deposition [57]. For the GICE period, we use values from published compilations of North

453   American bentonites[5,19] (Supplementary Table 4), and for the HICE we collate ages from

454   published bentonites from China (Supplementary Table 5). For the period 455 – 450 Ma

455   (corresponding to period covering the GICE), we take the number of ash layers to be 100 based

456   on observations[19]. We assume these ash layers represent eruptions of VEI 8 due to the location

457   and characteristics of these bentonites, which constitute discrete centimetre-thick horizons

458   thousands of kilometres from any proposed source[16,19]. We assume each eruption contained on

459   average 1000 km^3 erupted material[18]. To estimate how much erupted material was ash, we use

460   a value of 50%, representing the likely proportions in Ultraplinian eruptions[18,21]. Since we are

461   only interested, in the first instance, in the ash which may directly supply P to the ocean, we

462   use an estimate of 50% ashfall in the ocean basins. This number is based upon estimates of

463   ashfall which has been subducted since the Ordovician, using isopachs constructed from North

464   American outcrops[18], and paleogeographic reconstructions which indicate volcanism was

465   linked to the opening of the Iapetus Ocean (Figure 2). For all variables used in equation 2, we

466   apply standard deviations of all variables set at 25% of the variable mean, unless stated

467   (Supplementary Table 6). 10,000 simulations of all variables were performed using the r

468   package *rtrucnnorm*, and outputs were used to reconstruct likely ash volumes (in km^3).

469   For the period 450 – 440 Ma (corresponding to period covering the HICE), a similar set

470   of likely values for variables was constructed using published data on Chinese bentonite

471   deposits[21]. In this case, we use 88 ash layers as our mean, derived from the subtraction of 16

472   Silurian ashes from a compilation of Late Ordovician–early Silurian Chinese bentonites[21,65].

473   We use 75% as the oceanic fraction because this volcanism was linked with subduction of the

474   Zhenge-Dapu Ocean (Figure 2), and so a high proportion will be deposited in this

475   environment[21]. Again, we apply standard deviations of 25% to each of these variables to

476   consider the uncertainty.

477   In both cases, to estimate ash density, and the amount of P contained in the original

478   ashes, we use measured values from Icelandic ashfall[32,33], with standard deviations derived from

479   the measurements. Using the ash volume estimates derived from these variables, and our

480   depletion factors, we simulate 10,000 iterations for total P supply for each period (in mole P),

481   using the following equation (Eq. 2):

482    $$P\ release\ (mole)\ = \left(\frac{V_{Ash} \times \rho_{Ash} \times P_{Ash} \times P_D}{30.97}\right) \times P_{ocean} \text{(Equation 2)}$$

483   where V_{Ash}, ρ_{Ash} and P_{Ash} are the volume of ash (in km^3), density of ash (in kg/m^3) and

484   phosphorus content in ash (in wt %). P_D is the depletion factor of phosphorus, P_{ocean} is the

485   proportion falling into the ocean and 30.97 is the molecular weight of P, to convert from grams

486   to moles. Such an exercise provides an absolute amount of P released for each period, but for

487   modelling purposes, we must convert our total P supply values into flux (in mol P myr^{-1}).

488   To do this, we develop a dataset of all reliably dated (i.e., excluding K-Ar or fission

489 track dates) bentonites of Late Ordovician age from across the two primary volcanic provinces,

490 China and North America/Baltica (Figure 2, refs. [5,20,21,26–29,65–80]). For each of the dates, we use

491 a Monte Carlo based approach to generate 10,000 possible ages, constrained by published age

492 and error values. We group the outputs of this exercise into 0.25 Myr bins and produce

493 probability density estimates for each bin (Fig. 1a, b). For each of the two volcanic provinces,

494 we average across each bin to result in a probability density of each 0.25 Myr period (Fig. 1c).

495 This exercise results in two distinct peaks, representing the most likely period of volcanism for

496 both provinces. For North America/Scandinavia, this peak is centred on 453.5 Ma. For China,

497 the volcanic peak occurs 444.0 Ma. To represent these events in the model we then use a

498 standard Gaussian curve with σ=0.4, giving an event duration of around 2 Myrs. This width is

499 informed by the duration of the carbon isotope excursions.

500 **Estimating P flux from weathering**

501   We estimate the spatial extent of erupted material during the Late Ordovician using an

502 averaged value from a modelling study of Ordovician volcanism (1.56×10^6 km^2; ref.[60]). We

503 then use P release value of 29.77 kg P km^{-2} yr^{-1} as measured from basalts[82]. We estimate that

504 50% of the ash and lava was terrestrially emplaced based on the observations of ash deposition

505 considered previously[18,21]. By applying 20% errors to all of these values, we then carried out

506 10,000 Monte Carlo simulations of each variable, before calculating the final flux (in mol P

507 myr^{-1}) by multiplying each iteration of each variable.

508 **Biogeochemical modelling**

509   We use the latest COPSE biogeochemical model[39]. We run the model baseline and add

510 P_{force} to the global bioavailable phosphorus weathering flux (Equation 3). This adds additional

511 phosphorus input during the Late Ordovician to the baseline model run.

512 $$P_{force} = 10^{-6} P_{GICE} \frac{norm(t,-453.45,0.4)}{norm(-453.45,-453.45,0.4)} + 10^{-6} P_{HICE} \frac{norm(t,-444,0.4)}{norm(-444,-444,0.4)} \text{ (Eq. 3)}$$

513 Here P_{GICE} and P_{HICE} are the total P inputs from ash, weathering, and recycling in moles. Here

514 *norm* is a normal function defined as *norm(time,midpoint,σ)*. P_{force} is multiplied by 5 in some

515 simulations to represent the additional recycling of P which is not captured in the COPSE

516 model. This factor is determined by running a P-C cycling model which has an explicit

517 representation of the shelf[43] and comparing the ratio between P input from weathering and

518 overall marine P concentration versus the same metric in COPSE. The reader is referred to

519 Extended Data Figure 3 for the model comparison plots.

520 **Data Availability**

521 The authors declare that data supporting the findings of this study are available within the article

522 and Supplementary Information and Extended Data. All data have also been uploaded to

523 Figshare, at the following DOI addresses: http://dx.doi.org/10.6084/m9.figshare.14914893,

524 http://dx.doi.org/10.6084/m9.figshare.14914911,

525 http://dx.doi.org/10.6084/m9.figshare.14914896 and

526 http://dx.doi.org/10.6084/m9.figshare.14914890.

527 **Code availability**

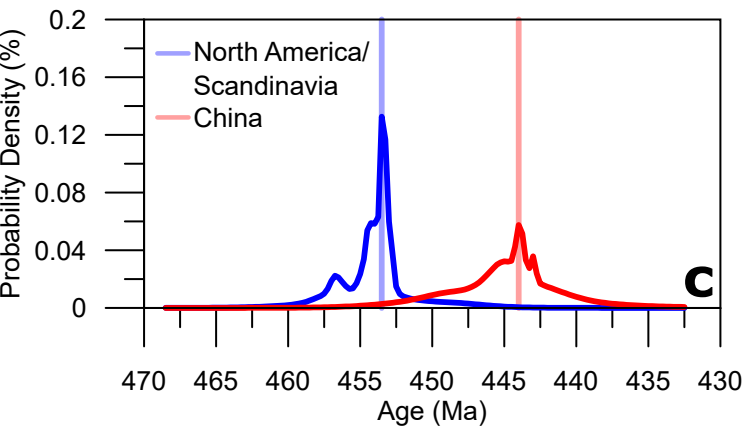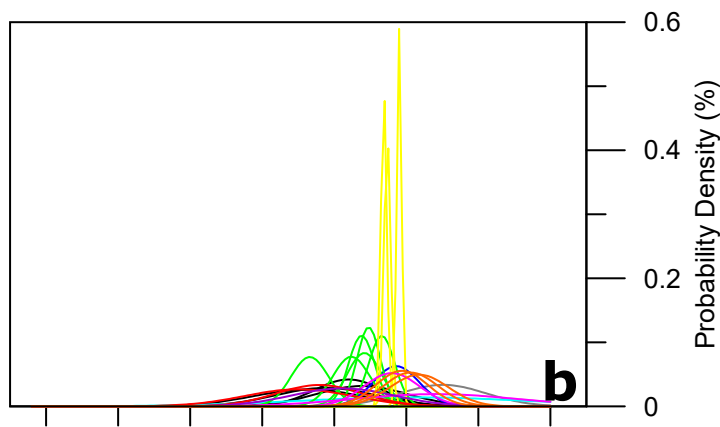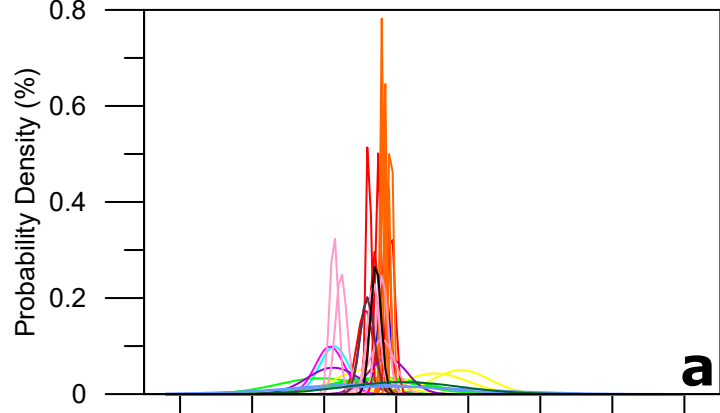528 COPSE model code can be downloaded at https://github.com/bjwmills

529 **Methods-only References**

530 58. Bitschene, P. R., Mehl, K. W. & Schmincke, H.-U. Composition and origin of marine ash layers

531 and epiclastic rocks from the Kerguelen Plateau, southern Indian Ocean (Legs 119 and 120). Proc. Ocean

532 Drill. Program, 120 Sci. Results 120, 135–149 (1992).

533 59. Schindlbeck, J. C. et al. One Million Years tephra record at IODP Sites U1436 and U1437:

534 Insights into explosive volcanism from the Japan and Izu arcs. Isl. Arc 27, e12244 (2018).

535   60.   Rodehorst, U., Schmincke, H.-U. & Sumita, M. Geochemistry and petrology of Pleistocene ash

536   layers erupted at Las Cañadas Edifice (Tenerife),. Scientific Results vol. 157 (1998).

537   61.   Salisbury, M. J. et al. Deep-sea ash layers reveal evidence for large, late Pleistocene and

538   Holocene explosive activity from Sumatra, Indonesia. J. Volcanol. Geotherm. Res. 231–232, 61–71

539   (2012).

540   62.   Derkachev, A. N. et al. Tephra layers of in the quaternary deposits of the Sea of Okhotsk:

541   Distribution, composition, age and volcanic sources. Quat. Int. 425, 248–272 (2016).

542   63.   Schindlbeck, J. C. et al. Late Cenozoic tephrostratigraphy offshore the southern Central

543   American Volcanic Arc: 1. Tephra ages and provenance. Geochemistry, Geophys. Geosystems 17,

544   4641–4668 (2016).

545   64.   Allan, A. S. R., Baker, J. A., Carter, L. & Wysoczanksi, R. J. Reconstructing the Quaternary

546   evolution of the world's most active silicic volcanic system: insights from an ~1.65 Ma deep ocean

547   tephra record sourced from Taupo Volcanic Zone, New Zealand. Quat. Sci. Rev. 27, 2341–2360 (2008).

548   65.   Yang, S. et al. Duration, evolution, and implications of volcanic activity across the Ordovician–

549   Silurian transition in the Lower Yangtze region, South China. Earth Planet. Sci. Lett. 518, 13–25 (2019).

550   66.   Tucker, R. D. U-Pb dating of Plinian-eruption ashfalls by the isotopic dilution method: a reliable

551   and precise tool for time-scale calibration and biostratigraphic correlation. Geol. Soc. Amer. Abs. w/

552   Prog. 24, A192 (1992).

553   67.   Oruche, N. E., Dix, G. R. & Kamo, S. L. Lithostratigraphy of the upper Turinian – Lower

554   Chatfieldian (upper Ordovician) foreland succession, and a U–Pb ID–TIMS date for the Millbrig

555   volcanic ash bed in the Ottawa embayment. Can. J. Earth Sci. 55, 1079–1102 (2018).

556   68.   Min, K., Renne, P. R. & Huff, W. D. Ar/Ar dating of Ordovician K-bentonites in Laurentia and

557   Baltoscandia. Earth Planet. Sci. Lett. 185, 121–134 (2001).

558   69.   Samson, S. D., Patchett, P. J., Roddick, J. C. & Parrish, R. R. Origin and tectonic setting of

559   Ordovician bentonites in North America: isotopic and age constraints. Geol. Soc. Am. Bull. 101, 1175–

560   1181 (1989).

561   70.   Svensen, H. H., Hammer, Ø. & Corfu, F. Astronomically forced cyclicity in the Upper

562   Ordovician and U-Pb ages of interlayered tephra, Oslo Region, Norway. Palaeogeogr. Palaeoclimatol.

563   Palaeoecol. 418, 150–159 (2015).

564   71.   Bauert, H. et al. New U-Pb zircon ages of the Sandbian (Upper Ordovician) 'Big K-bentonite'

565   in Baltoscandia (Estonia and Sweden) by LA-ICPMS. GFF 136, 30–33 (2014).

566   72.   Compston, W. & Williams, I. S. Ion probe ages for the British Ordovician and Silurian

567   stratotypes. in Global perspectives on Ordovician geology (eds. Webby, B. D. & Laurie, J. R.) 59–67

568   (1992).

569   73.   Li, Y., Zhang, T., Shao, D. & Shen, B. New U-Pb zircon age and carbon isotope records from

570   the Lower Silurian Longmaxi Formation on the Yangtze Platform, South China: Implications for

571   stratigraphic correlation and environmental change. Chem. Geol. 509, 249–260 (2019).

572   74.   Hu, Y. H., Zhou, J. Bin, Song, B., Li, W. & Sun, W. D. SHRIMP zircon U-Pb dating from K-

573   bentonite in the top of Ordovician of Wangjiawan section, Yichang, Hubei, China. Sci. China, Ser. D

574   Earth Sci. 51, 493–498 (2008).

575   75.   Xie, S., Wang, Z., Wang, J. & Zhuo, J. LA-ICP-MS zircon U-Pb dating of the bentonites from

576   the uppermost part of the Ordovician Wufeng Formation in the Haoping section,Taoyuan,Hunan.

577   Sediment. Tethyan Geol. 4, 597 (2012).

578   76.   Yang, S. et al. Constraints on the accumulation of organic matter in Upper Ordovician-lower

579   Silurian black shales from the Lower Yangtze region, South China. Mar. Pet. Geol. 120, 104544 (2020).

580   77.   Ge, X. et al. Mineralogical and geochemical characteristics of K-bentonites from the Late

581   Ordovician to the Early Silurian in South China and their geological significance. Geol. J. 54, 514–528

582   (2019).

583   78.   Zheng, B. et al. Nature of the Late Ordovician-Early Silurian Xiaohe section, Hunan-Hubei area,

584   South China: implications for the Kwangsian Orogeny. Int. Geol. Rev. 62, 1262–1272 (2020).

585   79.   Kunk, M. J., Sutter, J., Obradovich, J. D. & Lanphere, M. A. Age of biostratigraphic horizons

586   within the Ordovician and Silurian systems. Geol. Soc. Mem. 10, 89–92 (1985).

587   80.   Tucker, R. D., Krogh, T. E., Ross, R. J. & Williams, S. H. Time-scale calibration by high-

588   precision UPb zircon dating of interstratified volcanic ashes in the Ordovician and Lower Silurian

589   stratotypes of Britain. Earth Planet. Sci. Lett. 100, 51–58 (1990).

590   81.   Lefebvre, V., Servais, T., François, L. & Averbuch, O. Did a Katian large igneous province

591   trigger the Late Ordovician glaciation?. A hypothesis tested with a carbon cycle model. Palaeogeogr.

592   Palaeoclimatol. Palaeoecol. 296, 310–319 (2010).

593   82.   Hartmann, J., Moosdorf, N., Lauerwald, R., Hinderer, M. & West, A. J. Global chemical

594   weathering and associated p-release - the role of lithology, temperature and soil properties. Chem. Geol.

595   363, 145–163 (2014).

450 Ma

a

Phosphorus depletion (%)

1. Central America
2. Lesser Antilles
3. Canary Islands
4. Kergeulan
5. Sunda
6. Aleutians
7. Kyushu-Ryukyu
8. Taupo
9. Kamchatka/Kurile
10. Izu Bonin
All

100
50
0
-50
-100

b